

Received: 31 May 2021 Revised: 19 July 2021 Accepted: 23 July 2021

# Borohydride oxidation electrocatalysis at individual, shape-controlled Au nanoparticles

Partha Saha | Md. Maksudur Rahman | Caleb M. Hill

Department of Chemistry, University of Wyoming, Laramie, Wyoming, USA

### Correspondence

Caleb M. Hill, Department of Chemistry, University of Wyoming, 1000 E. University Ave., Laramie, WY 82071, USA. Email: caleb.hill@uwyo.edu

### Funding information

Wyoming NASA Space Grant Consortium, Grant/Award Number: NNX15AI08H; National Science Foundation, Grant/Award Number: CHE-2045593

### **Abstract**

Nanostructured materials are frequently employed as active components in electrochemical devices for energy conversion and storage. Unfortunately, the complexity of nanostructured materials, which can exhibit significant heterogeneities in morphology and/or composition within a macroscopic sample, makes it difficult to generate fundamental insights into their operation using traditional experimental techniques. Analytical methods that can probe the behavior of individual, discrete reactive entities, such as nanoparticles (NPs), may serve as powerful tools for the study of complex, heterogeneous systems, but remain experimentally challenging. Here, the application of probe-based electroanalytical methods is demonstrated to be a powerful, high-throughput strategy for the characterization of electrocatalytic systems. A pipet-based approach, Targeted Electrochemical Cell Microscopy (TECCM), was applied to characterize the electrocatalytic properties of individual, shape-controlled Au NPs toward the borohydride oxidation reaction (BOR), a model fuel cell reaction. Using TECCM, the BOR could be quantitatively interrogated at individual NPs in a high-throughput fashion, directly revealing significant NP-to-NP variations in reactivity and stability. BOR kinetics were found to exhibit a significant shape dependence, generally increasing in the order Triangles < Spheres  $\approx$ Octahedra < Rods, and prominent voltammetric features were observed that could be attributed to surface deactivation/reactivation process occurring at individual NPs. Together, these results demonstrate the large degree to which catalytic behavior varies at the single NP level and the power of applying single NP analytical techniques to the study of these systems.

#### KEYWORDS

electrocatalysis, electrochemical microscopy, nanoparticles, single-entity analysis

### 1 | INTRODUCTION

Elucidating structure-function relationships that rationally explain the electrochemical behavior of materials, particularly complex, heterogeneous, and/or nanostructured materials that may possess properties unique to that of their bulk counterparts, is an overarching goal of the electrochemical community with important

This is an open access article under the terms of the Creative Commons Attribution License, which permits use, distribution and reproduction in any medium, provided the original work is properly cited.

© 2021 The Authors. Electrochemical Science Advances published by Wiley-VCH GmbH



practical implications in catalysis, solar energy generation, and sensing. A central challenge that continues to impede these efforts is the difficulty associated with studying the chemical behavior of electrode surfaces, which is dictated by an enormous, randomly distributed ensemble of Å- to nm-scale structural motifs, using traditional, mm-scale experimental techniques. These techniques, such as voltammetry employing traditional micrometerto millimeter-scale electrodes, ultimately probe the collective activity of millions of discrete catalytic sites, particles. molecules, and so on, on the electrode surface, effectively "averaging out" valuable information that could help in the rational design of novel materials for electrochemical applications.

This difficulty could potentially be addressed through the design and implementation of analytical methods capable of probing individual, discrete reactive entities.[1] This strategy has been increasing in popularity in recent years, and a variety of experimental strategies capable of probing the electrochemical behavior of single entities have been demonstrated which utilize optical or electrochemical detection schemes. Optical methods, such as fluorescence, [2-5] dark field scattering, [6-14] electrogenerated chemiluminescence, [15,16] or plasmonic [17-22] imaging have been employed to track a variety of electrochemical processes occurring at individual nanostructures. Unfortunately, these approaches are often severely limited in terms of applicability and deducing electrochemical reaction rates from optical data is seldom straightforward. Direct electrochemical detection schemes are thus generally preferable, particularly probe-based schemes that can analyze the properties of individual entities in a rigorous, in-place fashion. A variety of strategies based on ultramicroelectrodes have been demonstrated at the single entity level, including "collision"-based techniques, [23-33] entity immobilization, [34,35] or scanning electrochemical microscopy (SECM).[36-42]

Scanning electrochemical cell microscopy (SECCM), [43-47] a comparatively new, but now wellestablished, technique that employs electrolyte-filled pipets as functional electrochemical probes, has been demonstrated as a particularly powerful tool for carrying out electrochemical studies at the single-entity level. SECCM has been successfully applied to characterize variations in catalytic activity within a variety of nanostructured catalyst materials, [48-60] photoelectrochemical processes at semiconducting materials, [61-65] nucleation processes, [66-68] and to characterize the catalytic properties of individual colloidal nanostructures. [69] Recently, our research group has demonstrated a variant of this approach that combines SECCM with optical mapping, allowing entities of interest within a sample to be iden-

tified and interrogated in a targeted fashion, rather than following traditional, scanning-based schemes.<sup>[70–72]</sup> This approach, "Targeted" Electrochemical Cell Microscopy (TECCM), enables the rigorous, direct electrochemical characterization afforded by SECCM to be applied in a high-throughput fashion, generating a wealth of single NP data which can be analyzed to reveal how electrochemical behavior varies within heterogeneous materials systems. In this report, TECCM is applied to quantify the rate of borohydride oxidation, a model fuel cell reaction, at individual Au nanoparticle (NP) catalysts of varying geometry. Using TECCM, this electrocatalytic transformation was interrogated at hundreds of individual NPs, directly revealing the significant NP-to-NP variations in catalytic rates and stability that are present in this seemingly simple system.

### **EXPERIMENTAL METHODS**

### 2.1 | Nanoparticle synthesis and characterization

AuNPs with spherical, rod-like, octahedral, and triangular geometries were synthesized following established seedmediated growth procedures, [73-76] details of which are provided in the Supporting Information. After synthesis, the NPs were characterized through a combination of UV-Visible extinction spectroscopy (Shimadzu 1650) and transmission electron microscopy (TEM, FEI Tecnai G2 F20, 200 keV) or scanning electron microscopy (SEM, JEOL 6500, 30 keV).

#### 2.2 Sample preparation

Indium tin oxide (ITO) coated glass coverslips (#1.5, 15–30  $\Omega$  sq<sup>-1</sup>, 22 × 22 mm, SPI) were cleaned by sequential sonication in deionized (DI) H2O, ethanol, and 2-propanol for 10 min each and rinsed with DI H<sub>2</sub>O. After drying, the ITO substrates were subjected to UV-O<sub>3</sub> cleaning for 5 min (Novascan PSD-UV) before NP deposition. Au NPs were deposited onto the cleaned ITO substrates by first diluting 100 µL of the synthesized NP solution to 1 mL with DI H<sub>2</sub>O in a 1 mL centrifuge tube. This diluted NP dispersion was then centrifuged twice at 11,000 g for 5 min at 30°C, replacing 900 μL of the supernatant with DI H<sub>2</sub>O each time. Five microliters of this purified NP dispersion was then dropped onto a clean ITO substrate and allowed to remain in contact for 5 min before rinsing the sample liberally with DI H<sub>2</sub>O. This procedure typically resulted in a NP density of  $\sim 0.1 \ \mu m^{-2}$  on the sample surface. The



sample was again subjected to UV-O<sub>3</sub> cleaning for 30 min to remove residual ligands on the NP surface.

### 2.3 | Bulk electrochemical measurements

Bulk electrochemical measurements were obtained using a traditional three-electrode cell and a potentio-stat (Gamry Reference 600). In all measurements, the working electrode was a 2 mm diameter Au inlaid disk electrode, the counter electrode was a Pt wire, and a Ag/AgCl (3 M KCl) electrode served as the reference electrode. All solutions employed for electrochemical measurements were prepared with DI  $\rm H_2O$  (> 18 M $\Omega$  cm, MilliQ Direct- $\rm Q^{\tiny (2)}5UV$ -R).

## 2.4 | Targeted electrochemical cell microscopy measurements

Targeted electrochemical cell microscopy (TECCM) was employed to probe the electrochemical properties of individual NPs, which has been described in detail elsewhere. [70-72] In brief, ITO-supported Au NP samples were mounted onto an inverted optical microscope and NPs of interest were identified using dark field imaging. A pipet with terminal dimensions on the order of 1 µm containing an aqueous electrolyte (100 mM NaOH and 10 mM NaBH<sub>4</sub>) and a AgCl-coated Ag wire was then brought into contact with the identified NPs using a piezo system. During translation of the probe, a bias was applied between the ITO substrate and AgCl wire and the current flowing through the system monitored using a patch clamp style amplifier (Dagan Chem Clamp). A sudden spike of current was observed upon probe-sample contact, at which point probe movement was stopped and a voltammogram obtained. Upon completion of the measurement, the probe was retracted and the cycle repeated for a different NP. This location and interrogation process enables individual NPs to be characterized at a rate of about 5 min<sup>-1</sup>. The potential and stability of the Ag/AgCl quasireference electrode was confirmed via potentiometric measurements versus a conventional Ag/AgCl (3 M KCl) reference electrode. The quasireference potential was found to be stable to within 20 mV over an hour-long period. Potentials in all TECCM measurements are reported versus the conventional Ag/AgCl (3 M KCl) reference potential. More details on the experimental setup, probe fabrication, characterization, and potential correction procedure are provided in the Supporting Information.

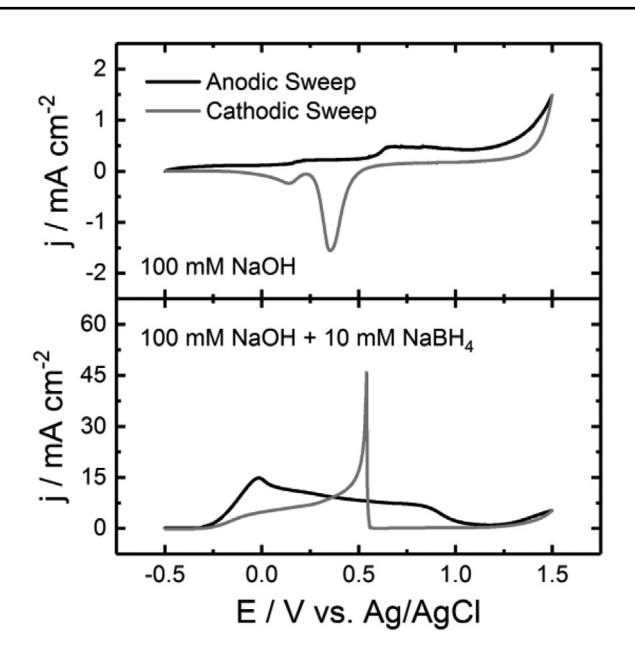


FIGURE 1 Cyclic voltammetry (100 mV/s) of a macroscopic polycrystalline Au electrode (r=1 mm) in aqueous solutions containing 100 mM NaOH with (bottom) or without (top) 10 mM NaBH<sub>4</sub>. Black and grey lines denote anodic and cathodic sweeps, respectively. Data are shown for the first potential cycle. Additional cycles in solutions containing borohydride are provided in Figure S3 in the Supporting Information

### 3 | RESULTS AND DISCUSSION

# 3.1 | Borohydride oxidation at bulk, polycrystalline Au

In order to provide context for the single NP studies, borohydride oxidation was first interrogated at a bulk, polycrystalline Au electrode. Cyclic voltammograms obtained with a macroscopic Au electrode in basic solutions (100 mM NaOH) in the absence and presence of  $BH_4^-$  are provided in Figure 1. In the absence of  $BH_4^-$ , the primary features observed are those associated with the formation and elimination of oxide films on the Au surface. An anodic wave is observed for potentials >0.6 V versus Ag/AgCl reflecting the formation of Au oxide, and a cathodic peak is observed at ca. 0.4 V corresponding to the reduction of the oxide layer to Au.  $^{[77]}$  These well-known processes can be summarized through the following equation:

$$2Au + 6OH^- \rightleftharpoons Au_2O_3 + 3H_2O + 6e^-$$

Additional features can also be observed associated with oxygen evolution (>1.2 V) and oxygen reduction (<0.2 V). In the presence of 10 mM  $BH_4^-$ , these features are largely unobservable. Here, the response is dominated by the

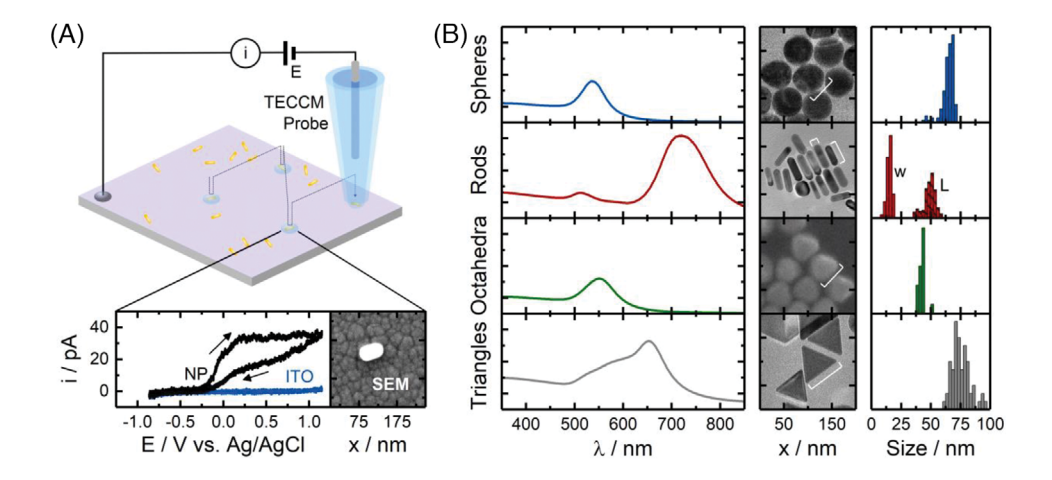


FIGURE 2 (A) Experimental schematic for TECCM. An electrolyte-filled pipet containing a Ag/AgCl counter electrode is brought into contact with a sample over an electroactive entity of interest and voltammetric measurements are obtained which reflect its activity. The inset provides an example cyclic voltammogram obtained at an individual Au nanorod in an aqueous solution of 10 mM NaBH $_4$  and 100 mM NaOH. A correlated SEM image of the same nanorod is also provided. (B) UV-Visible extinction spectra, representative electron microscopy images, and size distributions obtained for the colloidal Au NPs employed in this work. The relevant size parameter for each geometry is indicated in the corresponding electron microscopy image

oxidation of BH<sub>4</sub>-:

$$BH_4^- + 8OH^- \rightarrow BO_2^- + 6H_2O + 8e^-$$

In the initial anodic sweep, two features can be clearly identified: (a) an irreversible peak at ca. 0 V and (b) a decrease in current density around 0.9 V. Analysis of the anodic peak under the assumption of a rate controlling  $10^{-1}$  oxidation step (see SI for details) is consistent with the borohydride oxidation reaction (BOR) as described above and previous studies of borohydride oxidation at Au. [78,79] Based on the position and shape of the anodic peak, an effective standard rate constant ( $10^{-11}$  cm/s and 0.62, respectively. The loss of BOR activity above 0.9 V reflects a deactivation of the Au surface due to oxide formation.

During the cathodic sweep, a sudden onset of anodic current is observed near 0.5 V, which coincides with the onset of Au oxide reduction. Removal of the oxide film during the cathodic sweep thus "reactivates" the Au surface for BOR, causing a potential step-like response. These deactivation/reactivation processes have been previously described by other authors. [79–83]

### 3.2 | BOR at Single NPs

The goal of the present study was to interrogate BOR electrocatalysis at the single NP level, examining how catalytic efficiency and catalyst deactivation/reactivation processes vary at this scale. The experimental strategy employed was Targeted Electrochemical Cell Microscopy (TECCM),

a variant of Electrochemical Cell Microscopy recently demonstrated by the authors' laboratory. [70-72] The general principle of TECCM is depicted in Figure 2A. NPs of interest are immobilized onto a transparent electrode with poor catalytic properties (here indium tin oxide, ITO). An electrochemical probe consisting of a AgCl-coated Ag wire immersed in an electrolyte-filled pipet is then brought into contact with a sample at locations where individual NPs of interest reside. For the Au NPs employed here, these locations can be generated via dark field optical imaging due to the strong plasmon resonances exhibited by the particles. Probe-sample contact creates a miniaturized electrochemical cell centered around the NP of interest, and voltammetric measurements can then be obtained that directly reflect the catalytic properties of the NP due to the comparatively poor catalytic properties of the underlying substrate. A demonstration of this is provided in the inset of Figure 2A, which depicts a CV showing BH<sub>4</sub> oxidation at an individual Au NR. Correlated SEM imaging of the sample within the interrogated region was carried out to conclusively demonstrate TECCM measurements can reflect the properties of the individual, well-defined nanostructures of interest here.

In these studies, the catalytic properties of four distinct NP geometries, spheres, rods, octahedra, and triangular prisms (triangles), toward the BOR was explored at the single NP level using TECCM. All were synthesized using established seed-mediated growth procedures employing alkylammonium-based ligands. Optical extinction spectra (reflecting the surface plasmon resonances displayed by the NPs) and electron microscopy analyses of the NPs employed here are summarized in Figure 2B. Example

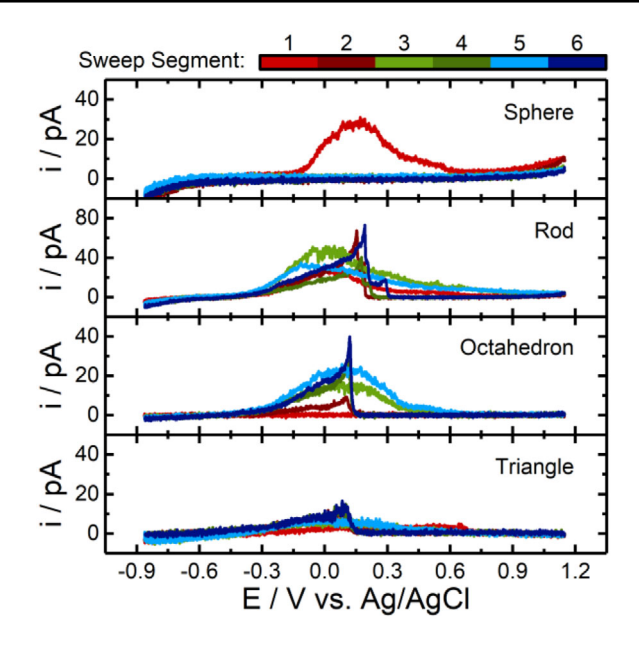


FIGURE 3 Example voltammograms depicting borohydride oxidation at individual NPs of varying geometry. Measurements were obtained using  $\sim\!\!1.0~\mu m$  diameter pipets filled with an aqueous solution of 10 mM NaBH $_4$  and 100 mM NaOH at a sweep rate of 1000 mV/s. The initial sweep was in the anodic direction, and successive sweep segments are denoted using different colors

BOR CVs obtained at individual NPs of each geometry are depicted in Figure 3 (additional examples are provided in Figure S4 in the Supporting Information). Two features were generally observed in the single NP TECCM measurements. During anodic sweeps, an anodic current wave could be observed, usually initiating between -0.3 and 0 V versus Ag/AgCl and decaying in intensity above ca. 0.3 V versus Ag/AgCl. During the cathodic sweeps, sudden onsets in anodic current were observed at some NPs, similar to those at bulk Au, usually between 0.1 and 0.3 V versus Ag/AgCl.

It is notable that the maximum BOR currents observed at individual NPs here are much lower than those one would expect on the basis of mass transfer to the NP surface. Previous work from our group has shown that mass transfer coefficients for NPs in the TECCM geometry are roughly half of that for NPs in an infinite volume of solution. [70] For a spherical NP supported on a planar substrate, the diffusion-limited current is as follows: [24]

$$i = 4\pi (\ln 2) nFDC^* r_0$$

where n is the number of electrons transferred in the reaction, F is the Faraday, D is the diffusion coefficient of the limiting redox active species (assumed here to be  $BH_4^-$ ),  $C^*$  is its bulk concentration, and  $r_0$  is the NP radius. Using

n = 8,  $D = 1.6 \times 10^{-5}$  cm<sup>2</sup>/s,<sup>[78]</sup> and  $r_0 = 30$  nm in the above equation yields ca. 3 nA, which is roughly two orders of magnitude larger than the currents observed here.

The inability to drive the BOR to the mass transfer limit at the single NP level is likely attributable to the complicated mechanism the reaction follows on Au, which despite numerous experimental and computational studies, [78–87] has not been definitively established. The experimental results presented here, particularly the observation of limiting currents well below the mass transfer limit, here can be qualitatively explained through the following generic mechanism:

$$BH_4^- + S \to A^* + n_1 e^- \quad (k_1, \text{ cm s}^{-1})$$

$$A^* \to B^* \quad (k_2, \text{ s}^{-1})$$

$$B^* \to BO_2^- + S + (8 - n_1)e^- \quad (\text{Fast})$$

$$S \rightleftharpoons O^* \quad (k_3/k_{-3}, \text{ s}^{-1})$$

Here, BH<sub>4</sub> in solution is first oxidized at a vacant surface site, S, to create an adsorbed species, A\*. This adsorbed species undergoes a surface chemical reaction to produce another adsorbed species, B\*, which subsequently undergoes a series of fast steps to produce the final BO<sub>2</sub> product and a vacant surface site. Meanwhile, vacant sites on the Au surface can also be reversibly occupied through formation/elimination of Au oxides. Finite element simulations were carried out to compare the observed experimental results against this mechanism, assuming the rates of the initial electron transfer and oxide formation reactions ( $k_1$ and  $k_3/k_{-3}$ ) follow traditional Butler-Volmer expressions for a one electron transfer and the rate of the surface reaction step,  $k_2$ , is constant. Butler-Volmer parameters for  $k_1$ were generated through analysis of the initial anodic wave depicted in Figure 3. Parameters for  $k_3/k_{-3}$  were varied in the finite element simulations to reproduce the deactivation/reactivation features observed at bulk Au, while  $k_2$ was varied to reproduce the limiting currents observed in TECCM measurements. Additional details on these simulations are provided in the Supporting Information.

Results from the simulations are provided in Figure 4. At bulk Au, the experimental behavior could be reproduced well, with oxide formation/elimination accounting for both the deactivation near 0.9 V in the anodic sweep and the step-like response near 0.5 V in the cathodic sweep. The bulk response was also relatively insensitive to the rate of the surface process,  $k_2$ . Simulations carried out at a spherical NP (30 nm radius) in the TECCM geometry exhibited several differences. The onset of BOR current

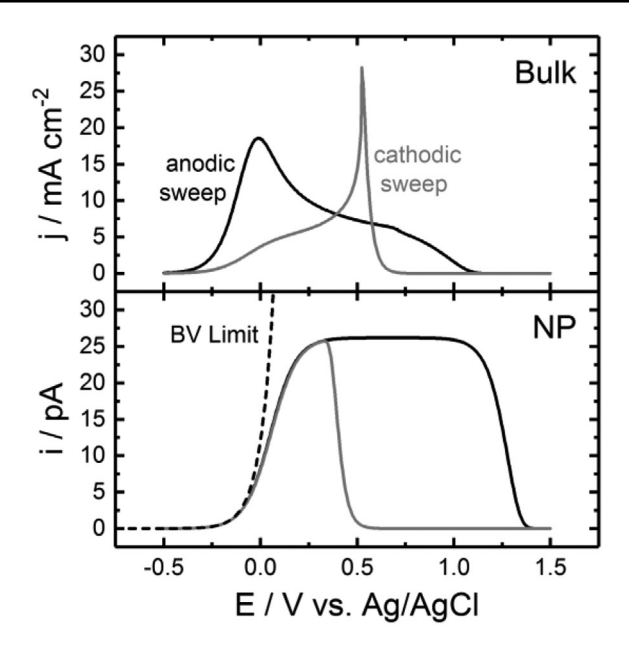


**FIGURE 4** Finite element simulations of BOR voltammetry at bulk Au ( $\nu = 100 \text{ mV/s}$ ) and a spherical Au NP ( $\nu = 1000 \text{ mV/s}$ ,  $r_0 = 30 \text{ nm}$ ) interrogated in the TECCM geometry. Simulation methods and parameters employed are detailed in the Supporting Information

was shifted to positive potentials by several hundred mV due to the significantly higher mass transfer coefficients in effect in this geometry. BOR currents then increased to a limiting value, dictated by the value of  $k_2$ . As in the bulk case, deactivation was observed at more anodic potentials, lasting until a potential of ca. 0.5 V was reached in the cathodic sweep, at which point the current quickly returned to its limiting value. Good agreement with experimental data was observed for  $k_2$  values of ca.  $300 \, \mathrm{s}^{-1}$ .

While the voltammetric behavior discussed above is generally representative of all NPs interrogated via TECCM, there was a large degree of variability observed at the single NP level, both in terms of key parameters (e.g., onset potentials, peak currents) and how this behavior evolved over time. Some NPs were found to quickly deactivate (e.g., the sphere in Figure 3), while others were relatively stable (rod) or showed increased activity with successive cycling (octahedron or triangle). These dynamic changes in catalytic behavior are likely attributable to dynamic changes in the surface of the NP which occur during cycling (i.e., removal of residual alkylammonium ligands or poisoning of the surface), which are not explicitly addressed in the above mechanism. The observed catalytic behavior showed no significant relationship with measurement order (see Figure S5), however, suggesting adventitious impurities from the ambient air did not have any meaningful impact on the present experiments.

### 3.3 | Statistical analysis of single NP behavior

In order to gain further insights into the heterogeneity of the BOR process at the single NP level, statistical analyses were carried out on hundreds of individual NP interrogated via TECCM. In these analyses, the peak currents and onset potentials (defined as the potential at 5 pA anodic current) were chosen as the analyzed parameters. Statistical distributions in the peak BOR currents are given in Figure 5. The observed trends are generally similar for all particle geometries investigated. In the first cycle, broad distributions in peak currents are observed, reflecting a wide distribution in catalytic activity. In subsequent cycles, distributions shift to lower average currents, becoming exponential in shape and relatively stable. However, this "stability" is somewhat misleading due to the variability in NP behavior evident in Figure 3. The catalytic properties of the NPs toward the BOR are not static, as these distributions would seem to imply. Rather, the apparent stability arises from a balance in the number of particles activating and deactivating during cycling. Distributions for the onset potentials observed at individual NPs are provided in Figure 6. Here, the evolution in behavior is again relatively consistent among the investigated NP geometries. In the first cycle, onset potentials are generally observed below ca. -0.1 V for all NP geometries investigated. In subsequent cycles, these distributions widen and the average onset potentials shift to more positive values, reflecting a slight decrease in catalytic activity. Due to the similar behavior observed among different NP geometries, it is likely that the deactivation arises from the nonspecific adsorption of reaction products and/or impurities in the electrolyte solution that do not favor particular facets on Au.

These general trends are summarized in Figure 7, which gives the average peak currents, onset potentials, and effective heterogeneous rate constants (i.e.,  $k_1^0$ ) observed at individual NPs as a function of cycle number. The spread in observed onset potentials, spanning several hundred mV for each particle geometry investigated, was much larger than one would expect on the basis of variations in particle size alone ( $\sim$ 10 mV; see the Supporting Information for a detailed discussion of this point). The observed heterogeneity in onset potentials is thus attributed to variations in an effective heterogeneous rate constant,  $k^0$ , likely arising from variations in active NP surface area. These effective rate constants were calculated from the onset potential as:

$$k_1^0 = \frac{i_{5 pA}}{8FAC_R e^{\frac{(1-\alpha)F}{RT}} (E_{5 pA} - E^{0'})}$$

where  $i_{5 pA}$  is the current (5 pA), 8 is the number of total electrons transferred, A is the surface area of the

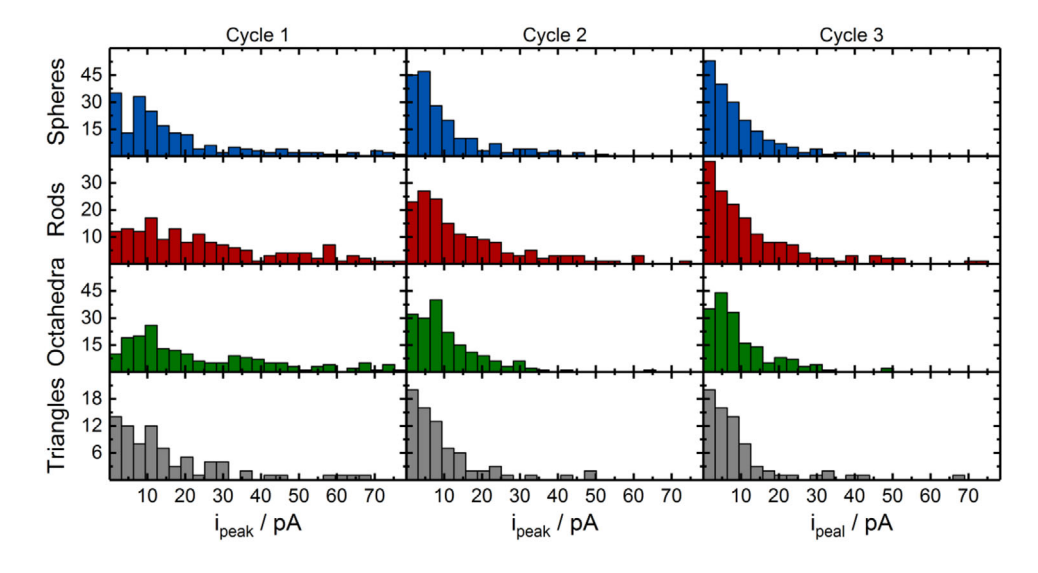


FIGURE 5 Statistical distribution in peak BOR currents observed at individual Au NPs interrogated via TECCM. Experimental conditions identical to those in Figure 3

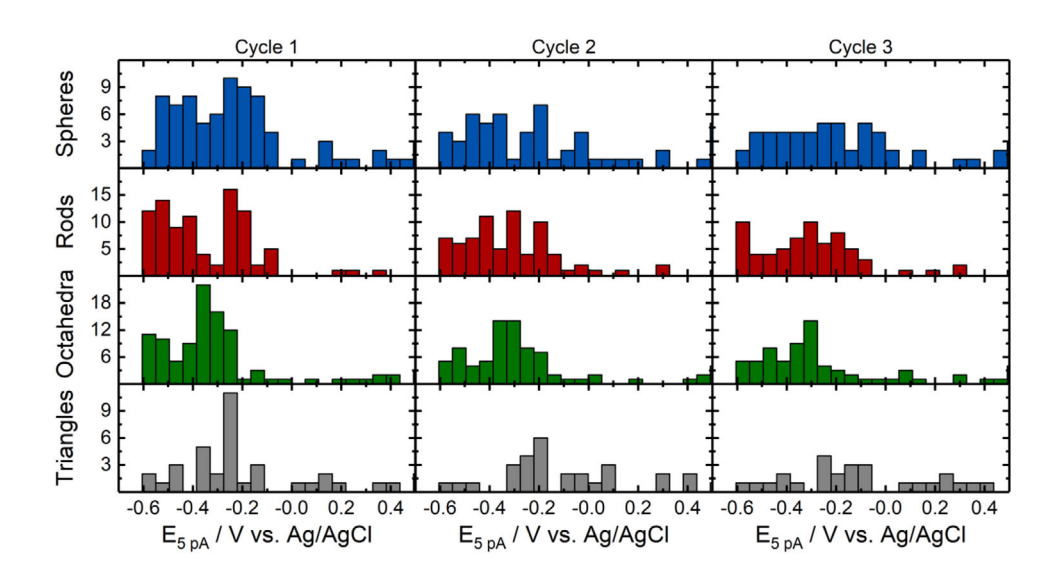


FIGURE 6 Statistical distribution in peak BOR onset potentials observed at individual Au NPs interrogated via TECCM. Onset potentials were defined as potential necessary to generate an anodic current of 5 pA. Experimental conditions identical to those in Figure 3

particle,  $C_R$  is the concentration of  $BH_4^-$ , RT is the gas constant times temperature, and  $E^{0'}$  is the formal potential of the rate-limiting electron transfer. The transfer coefficient,  $\alpha$ , was determined through analysis of the local slope of the voltammogram at the onset potential. Average  $\alpha$  values of  $0.62 \pm 0.05$ ,  $0.68 \pm 0.04$ ,  $0.60 \pm 0.04$ , and  $0.50 \pm 0.13$  were observed for spheres, rods, octahedra, and triangles, respectively, which did not exhibit statistically meaningful shifts during cycling. Interestingly, the nanorods exhibited average rate constants greater than those observed at bulk Au (ca.  $10^{-11}$  cm/s). The octahedra and nanospheres

were comparable in activity to bulk Au, while the triangular particles performed significantly worse. These differences in observed kinetic parameters can be attributed to differences in the faceting of the particle surface. While the spherical NPs employed here do not possess any significant degree of faceting, [73] morphologically "smooth" Au nanorods are known to exhibit high-index (e.g., {730}) facets that contain a high density of catalytically active, low-coordination sites. [88,89] The catalytic activity of the octahedral and triangular particles could be predicted to be lower as both are nominally dominated by lower energy

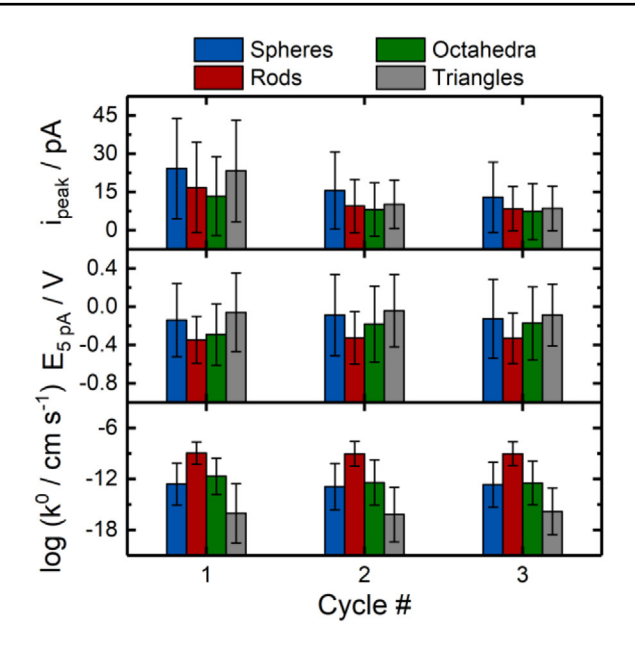


FIGURE 7 Summary of statistical averages in key parameters evaluated at individual Au NPs using TECCM. Error bars indicate ±1 standard deviation

{111} facets. However, the faceting of the octahedral NPs employed here was not as well-defined, explaining their observed similarity in behavior to the spherical NPs.

### 4 | CONCLUSIONS

In this report, the electrocatalytic activity of a variety of well-defined, colloidal Au NPs toward the borohydride oxidation reaction (BOR) was explored at the single NP level using Targeted Electrochemical Cell Microscopy (TECCM). Through the application of TECCM, voltammograms directly reflecting the BOR activity of discrete Au NPs could be generated in a high-throughput fashion, allowing statistically significant quantities of single NP data to be generated. These single NP responses displayed prominent features associated with the deactivation of the catalyst surface through reversible oxide formation. Qualitatively, the single NP responses were similar to those observed at bulk Au, but the currents observed at the single NP level were well below the mass transfer limit, likely due to a rate-limiting surface reaction. While the evolution in catalytic activity over time was heterogeneous at the single NP level, with some NPs increasing in activity and others decreasing, statistical trends were observed to be the same among the interrogated geometries. Using the single NP data, kinetic parameters for the BOR were calculated for the different geometries which show kinetic facility increases in the order Triangles < Spheres  $\approx$ Octahedra < Rods, which can be attributed to differences in the surface faceting of the NPs. Together, these results demonstrate the significant heterogeneity that is ubiquitous in the chemical behavior of nanostructured materials and the utility of single entity analytical techniques for studying these systems.

### **ACKNOWLEDGMENTS**

The authors acknowledge generous support for this work from the National Science Foundation (CHE-2045593), the University of Wyoming, and the Wyoming NASA Space Grant Consortium (NASA Grant #NNX15AI08H).

### DATA AVAILABILITY STATEMENT

All data from these studies is available upon request.

### REFERENCES

- 1. L. A. Baker, J. Am. Chem. Soc. 2018, 140, 15549.
- J. B. Sambur, T. Y. Chen, E. Choudhary, G. Chen, E. J. Nissen, E. M. Thomas, N. Zou, P. Chen, *Nature* 2016, 530, 77.
- N. Zou, X. Zhou, G. Chen, N. M. Andoy, W. Jung, G. Liu, P. Chen, Nat. Chem. 2018, 10, 607.
- X. Zhou, N. M. Andoy, G. Liu, E. Choudhary, K. S. Han, H. Shen, P. Chen, Nat. Nanotechnol. 2012, 7, 237.
- X. Zhou, W. Xu, G. Liu, D. Panda, P. Chen, J. Am. Chem. Soc. 2010, 132, 138.
- S. Hu, J. Yi, Y.-J. Zhang, K.-Q. Lin, B.-J. Liu, L. Chen, C. Zhan, Z.-C. Lei, J.-J. Sun, C. Zong, J.-F. Li, B. Ren, *Nat. Commun.* 2020, 11, 2518.
- 7. V. Brasiliense, J. Clausmeyer, A. L. Dauphin, J. M. Noël, P. Berto, G. Tessier, W. Schuhmann, F. Kanoufi, *Angew. Chemie Int. Ed.* **2017**, *56*, 10598.
- V. Brasiliense, P. Berto, C. Combellas, R. Kuszelewicz, G. Tessier, F. Kanoufi, Faraday Discuss.. 2016, 193, 339.
- 9. B. S. Hoener, H. Zhang, T. S. Heiderscheit, S. R. Kirchner, A. S. De Silva Indrasekara, R. Baiyasi, Y. Cai, P. Nordlander, S. Link, C. F. Landes, W.-S. Chang, *J. Phys. Chem. Lett.* **2017**, *8*, 2681.
- B. S. Hoener, C. P. Byers, T. S. Heiderscheit, A. S. De Silva Indrasekara, A. Hoggard, W. S. Chang, S. Link, C. F. Landes, *J. Phys. Chem. C* 2016, 120, 20604.
- 11. C. P. Byers, B. S. Hoener, W. S. Chang, S. Link, C. F. Landes, *Nano Lett.*. **2016**, *16*, 2314.
- C. Novo, A. M. Funston, A. K. Gooding, P. Mulvaney, J. Am. Chem. Soc. 2009, 131, 14664.
- V. Brasiliense, A. N. Patel, A. Martinez-Marrades, J. Shi, Y. Chen, C. Combellas, G. Tessier, F. Kanoufi, J. Am. Chem. Soc. 2016, 138, 3478.
- K. Wonner, M. V. Evers, K. Tschulik, J. Am. Chem. Soc. 2018, 140, 12658
- 15. S. Pan, J. Liu, C. M. Hill, J. Phys. Chem. C 2015, 119, 27095.
- 16. A. J. Wilson, K. Marchuk, K. A. Willets, Nano Lett.. 2015, 15, 6110.
- X. Shan, U. Patel, S. Wang, R. Iglesias, N. Tao, Science 2010, 327, 1363
- Y. Fang, W. Wang, X. Wo, Y. Luo, S. Yin, Y. Wang, X. Shan, N. Tao, J. Am. Chem. Soc. 2014, 136, 12584.
- X. Shan, I. Díez-Pérez, L. Wang, P. Wiktor, Y. Gu, L. Zhang, W. Wang, J. Lu, S. Wang, Q. Gong, J. Li, N. Tao, *Nat. Nanotechnol.* 2012, 7, 668.

Research article



- H. Wang, X. Shan, H. Yu, Y. Wang, W. Schmickler, H. Y. Chen, N. Tao, *Angew. Chem., Int. Ed.* 2017, 56, 2132.
- Y. Wang, X. Shan, H. Wang, S. Wang, N. Tao, J. Am. Chem. Soc. 2017, 139, 1376.
- 22. W. Wang, N. Tao, Anal. Chem. 2014, 86, 2.
- 23. X. Xiao, A. J. Bard, J. Am. Chem. Soc. 2007, 129, 9610.
- Y. Xiao, F. R. F. Fan, J. Zhou, A. J. Bard, J. Am. Chem. Soc. 2008, 130, 16669.
- 25. B. Roehrich, L. Sepunaru, Angew. Chem., Int. Ed. 2020, 59, 19184.
- 26. J. E. Dick, A. J. Bard, J. Am. Chem. Soc. 2015, 137, 13752.
- M. Zhou, J. E. Dick, A. J. Bard, J. Am. Chem. Soc. 2017, 139, 17677.
- 28. M. W. Glasscott, A. D. Pendergast, S. Goines, A. R. Bishop, A. T. Hoang, C. Renault, J. E. Dick, *Nat. Commun.* **2019**, *10*, 2650.
- 29. M. W. Glasscott, J. E. Dick, Anal. Chem. 2018, 90, 7804.
- A. D. Pendergast, C. Renault, J. E. Dick, Anal. Chem. 2021, 93, 2898
- M. W. Glasscott, C. M. Hill, J. E. Dick, J. Phys. Chem. C 2020, 124, 14380.
- K. J. Vannoy, A. Ryabykh, A. I. Chapoval, J. E. Dick, *Analyst* 2021, 146, 3413.
- A. D. Pendergast, Z. Deng, F. Maroun, C. Renault, J. E. Dick, ACS Nano 2021, 15, 1250.
- 34. Y. Li, J. T. Cox, B. Zhang, J. Am. Chem. Soc. 2010, 132, 3047.
- 35. T. J. Anderson, B. Zhang, Acc. Chem. Res. 2016, 49, 2625.
- 36. Y. Yu, T. Sun, M. V. Mirkin, Anal. Chem. 2015, 87, 7446.
- T. Sun, Y. Yu, B. J. Zacher, M. V. Mirkin, Angew. Chemie Int. Ed. 2014, 53, 14120.
- 38. P. Y. Blanchard, T. Sun, Y. Yu, Z. Wei, H. Matsui, M. V. Mirkin, *Langmuir* **2016**, *32*, 2500.
- T. Sun, D. Wang, M. V. Mirkin, H. Cheng, J.-C. Zheng, R. M. Richards, F. Lin, H. L. Xin, *Proc. Natl. Acad. Sci. USA* 2019, *116*, 201821091.
- 40. A. Djire, X. Wang, C. Xiao, O. C. Nwamba, M. V. Mirkin, N. R. Neale, *Adv. Funct. Mater.* 30, 2020, 2001136.
- J. Kim, C. Renault, N. Nioradze, N. Arroyo-Currás, K. C. Leonard, A. J. Bard, J. Am. Chem. Soc. 2016, 138, 8560.
- J. Kim, C. Renault, N. Nioradze, N. Arroyo-Currás, K. C. Leonard, A. J. Bard, Anal. Chem. 2016, 88, 10284.
- M. E. Snowden, A. G. Güell, S. C. S. Lai, K. McKelvey, N. Ebejer,
   O'M. A. Connell, A. W. Colburn, P. R. Unwin, *Anal. Chem.* 2012,
   84, 2483.
- 44. N. Ebejer, M. Schnippering, A. W. Colburn, M. A. Edwards, P. R. Unwin, *Anal. Chem.* **2010**, *82*, 9141.
- E. Daviddi, K. L. Gonos, A. W. Colburn, C. L. Bentley, P. R. Unwin, *Anal. Chem.* 2019, 91, 9229.
- 46. O. J. Wahab, M. Kang, P. R. Unwin, *Curr. Opin. Electrochem.* **2020**, *22*, 120.
- 47. N. Ebejer, A. G. Güell, S. C. S. Lai, K. McKelvey, M. E. Snowden, P. R. Unwin, *Annu. Rev. Anal. Chem.* **2013**, *6*, 329.
- 48. S. C. S. Lai, P. V. Dudin, J. V. MacPherson, P. R. Unwin, *J. Am. Chem. Soc. 133*, **2011**, 133, 10744.
- M. Kang, D. Perry, C. L. Bentley, G. West, A. Page, P. R. Unwin, ACS Nano 2017, 11, 9525.
- C. L. Bentley, M. Kang, F. M. Maddar, F. Li, M. Walker, J. Zhang,
   P. R. Unwin, *Chem. Sci.* 2017, 8, 6583.
- J. T. Mefford, A. R. Akbashev, M. Kang, C. L. Bentley, W. E. Gent,
   H. D. Deng, D. H. Alsem, Y.-S. Yu, N. J. Salmon, D. A. Shapiro,
   P. R. Unwin, W. C. Chueh, *Nature* 2021, 593, 67.

- E. Daviddi, Z. Chen, B. Beam Massani, J. Lee, C. L. Bentley, P. R. Unwin, E. L. Ratcliff, ACS Nano 2019, 13, 13271.
- C. L. Bentley, M. Kang, P. R. Unwin, J. Am. Chem. Soc. 2019, 141, 2179
- C. L. Bentley, M. Kang, P. R. Unwin, J. Am. Chem. Soc. 2017, 139, 16813.
- C. L. Bentley, J. Edmondson, G. N. Meloni, D. Perry, V. Shkirskiy,
   P. R. Unwin, *Anal. Chem.* 2019, 91, 84.
- L. C. Yule, V. Shkirskiy, J. Aarons, G. West, C. L. Bentley, B. A. Shollock, P. R. Unwin, *J. Phys. Chem. C* 2019, *123*, 24146.
- R. G. Mariano, M. Kang, O. J. Wahab, I. J. McPherson, J. A. Rabinowitz, P. R. Unwin, M. W. Kanan, Nat. Mater. 2021, 1.
- 58. A. G. Güell, K. E. Meadows, P. V. Dudin, N. Ebejer, J. V. Macpherson, P. R. Unwin, *Nano Lett.*. **2014**, *14*, 220.
- C. L. Bentley, C. Andronescu, M. Smialkowski, M. Kang, T. Tarnev, B. Marler, P. R. Unwin, U.-P. Apfel, W. Schuhmann, Angew. Chem., Int. Ed. 2018, 57, 4093.
- S. E. F. Kleijn, S. C. S. Lai, T. S. Miller, A. I. Yanson, M. T. M. Koper, P. R. Unwin, J. Am. Chem. Soc. 2012, 134, 18558.
- 61. J. W. Hill, C. M. Hill, Nano Lett.. 2019, 19, 5710.
- J. W. Hill, Z. Fu, J. Tian, C. M. Hill, J. Phys. Chem. C 2020, 124, 17141.
- L. E. Strange, J. Yadav, S. Garg, P. S. Shinde, J. W. Hill, C. M. Hill,
   P. Kung, S. Pan, J. Phys. Chem. Lett. 2020, 11, 3488.
- 64. J. W. Hill, C. M. Hill, Chem. Sci. 2021, 12, 5102.
- B. D. B. Aaronson, J. C. Byers, A. W. Colburn, K. McKelvey, P. R. Unwin, *Anal. Chem.* 2015, 87, 4129.
- 66. Y. Wang, E. Gordon, H. Ren, J. Phys. Chem. Lett. 2019, 10, 3887.
- Y. Liu, C. Jin, Y. Liu, K. H. Ruiz, H. Ren, Y. Fan, H. S. White, Q. Chen, ACS Sens. 2021, 6, 355.
- C. JIN, Y.-L. LIU, Y. SHAN, Q.-J. CHEN, Chinese J. Anal. Chem. 2021, 49, e21055.
- M. Choi, N. P. Siepser, S. Jeong, Y. Wang, G. Jagdale, X. Ye, L. A. Baker, *Nano Lett.*. 2020, 20, 1233.
- P. Saha, J. W. Hill, J. D. Walmsley, C. M. Hill, *Anal. Chem.* 2018, 90, 12832.
- J. D. Walmsley, J. W. Hill, P. Saha, C. M. Hill, J. Anal. Test. 2019, 3, 140.
- M. Maley, J. W. Hill, P. Saha, J. D. Walmsley, C. M. Hill, J. Phys. Chem. C 2019, 123, 12390.
- C. Hanske, G. González-Rubio, C. Hamon, P. Formentín, E. Modin, A. Chuvilin, A. Guerrero-Martínez, L. F. Marsal, L. M. Liz-Marzán, J. Phys. Chem. C 2017, 121, 10899.
- L. Scarabelli, M. Coronado-Puchau, J. J. Giner-Casares, J. Langer, L. M. Liz-Marzán, ACS Nano 2014, 8, 5833.
- 75. B. Nikoobakht, M. A. El-Sayed, Chem. Mater. 2003, 15, 1957.
- P.-J. Chung, L.-M. Lyu, M. H. Huang, Chem. A Eur. J. 2011, 17, 9746.
- 77. U. Oesch, J. Janata, Electrochim. Acta 1983, 28, 1247.
- M. V Mirkin; H. Yang, A. J. Bard, J. Electrochem. Soc. 1992, 139, 2212.
- M. Chatenet, M. B. Molina-Concha, J.-P. Diard, *Electrochim. Acta* 2009, 54, 1687.
- 80. A. Ignaszak, D. C. W. Kannangara, V. W. S. Lam, E. L. Gyenge, *J. Electrochem. Soc.* **2013**, *160*, H47.
- D. M. F. Santos, C. A. C. Sequeira, J. Electrochem. Soc. 2010, 157, F16.
- D. M. F. Santos, C. A. C. Sequeira, *Electrochim. Acta* 2010, 55, 6775.



 M. Chatenet, F. H. B. Lima, E. A. Ticianelli, *J. Electrochem. Soc.* 2010, *157*, B697.

10 of 10

- 84. D. M. F. Santos, C. A. C. Sequeira, *J. Electrochem. Soc.* **2009**, *156*, F67.
- 85. G. Rostamikia, M. J. Janik, J. Electrochem. Soc. 2009, 156, B86.
- 86. G. Rostamikia, A. J. Mendoza, M. A. Hickner, M. J. Janik, *J. Power Sources* **2011**, *196*, 9228.
- 87. D. A. Finkelstein, N. Mota J. L. Da; Cohen, H. D. Abruña, *J. Phys. Chem. C* **2009**, *113*, 19700.
- 88. Q. Zhang, L. Han, H. Jing, D. A. Blom, Y. Lin, H. L. Xin, H. Wang, ACS Nano **2016**, *10*, 2960.
- 89. X. Ye, C. Zheng, J. Chen, Y. Gao, C. B. Murray, *Nano Lett.*. **2013**, 13, 765

### SUPPORTING INFORMATION

Additional supporting information may be found online in the Supporting Information section at the end of the article.

**How to cite this article:** P. Saha, M. M. Rahman, C. M. Hill, *Electrochem. Sci. Adv.* **2021**, e2100120. https://doi.org/10.1002/elsa.202100120